The Impact of Real Roughness Features on Boundary Layer Transition

Sivaramakrishnan Malathi Ananth[1], Subhathra Sabapathy[2], Nagabhushana Rao Vadlamani[3*], John Coull[4]

[1-3]Department of Aerospace Engineering, Indian Institute of Technology Madras, Chennai, 600036, India.
[4]Department of Engineering Science, The University of Oxford, Oxford, OX1 3PJ, United Kingdom.

*Corresponding author(s). E-mail(s): nrv@iitm.ac.in;
Contributing authors: ananthsm@alumni.iitm.ac.in;
ae22m017@smail.iitm.ac.in; john.coull@eng.ox.ac.uk;

Abstract

In this work, the effects of realistic roughness scales on boundary layer transition are investigated using high-resolution scale-resolving simulations. This is in contrast to most of the roughness-induced transition studies reported in the literature based on ordered and well-defined surface roughness elements. Two highly irregular surface roughness patterns are generated from a given roughness patch by selectively filtering out the higher frequencies. The transitional behavior of a laminar boundary layer developing over these roughness scales is examined at $\boldsymbol{Re_{\delta^*_{in}} = 360}$ and **540**, defined in terms of the inflow velocity and inlet displacement thickness. The impact on transition is explored by examining the instantaneous and time-averaged flow fields. The results show that the transition onset is sensitive to the roughness scales: the inclusion of finer scales reduces the spacing between roughness features thereby constraining the lateral development of the flow. The streaks are weaker due to the mutual sheltering effect and the finer scales are shown to promote spanwise inhomogeneity of flow in the transition region. This effect is found to be much more prominent at low Reynolds numbers. In contrast, filtering out the finer roughness scales results in an earlier transition onset, caused by strong streaks developing from the horseshoe vortices wrapping around sparsely packed roughness features. Further cases are studied to investigate the spatial features of roughness that are important for transition. A series of high-fidelity simulations using selective retention of roughness features are performed at $\boldsymbol{Re_{\delta^*_{in}} = 360}$. The transition onset can be predicted satisfactorily by retaining the dominant scales (20 tallest peaks in this study) from the original rough surface while the valleys and fine-scale features are shown to have minimal effect. In addition, we demonstrate that modifying the roughness patch or Reynolds number during the simulation alters the transition onset, which gets quickly established within $\boldsymbol{\approx 1725 k_{rms}/U_{in}}$. These findings have the potential to reduce the computational cost and further aid in improving the transition correlations employed in low-fidelity simulations.

Keywords: Real roughness, transition, sheltering, scale-resolving

1 Introduction

Surface roughness degrades the aerodynamic performance of several engineering systems across a range of applications. Gas turbine components such as compressors and turbine blades are susceptible to various damage mechanisms during operation. Surface erosion and/or deposition on blades due to in-service degradation further increases the scales of roughness [1]. The result is a progressive increase in the specific fuel consumption throughout the life of the engine. Aerodynamically, roughness can increase losses by either (1) promoting early boundary layer transition [2] and/or (2) enhancing turbulent production in an already turbulent boundary layer [3]. This paper examines the first mechanism.

Many of the classical studies of roughness-induced transition focused on discrete roughness elements [4, 5]. Vadlamani et al. [6] employed Direct Numerical Simulations (DNS) to investigate the effect of distributed roughness on the spatial evolution of transitional and turbulent boundary layers. They observed that the roughness height significantly alters the underlying transition mechanism. The effects of realistic surface roughness on the mean flow and turbulent stresses were studied by Yuan and Piomelli [7] employing Large Eddy Simulations (LES). Their work examined the influence of the effective slope of the rough surface on the roughness function for various surfaces. The experimental work of Anand and Diwan [8] on boundary layer transition under random distributed roughness is noteworthy. They characterized the time-frequency behavior of a laminar boundary layer perturbed by sandpaper strips and investigated the transition characteristics under sub-critical and super-critical roughness based Reynolds numbers. Jeong et al. [9] performed hot wire measurements in a laminar boundary layer subjected to dynamically smooth and sand paper-type transitionally rough surfaces to investigate the detailed transition process under different levels of roughness height perturbations. They found that the latter induce early transition and shortens the transition length compared to the former.

Lu et al. [10] employed DNS to investigate the shielding effect introduced by a two-dimensional strip on the transition initiated by an isolated smooth-edged three-dimensional discrete roughness. They discovered that the downstream shielding weakens the strong streamwise vortices thereby inhibiting its lift-up effect and delaying the transition. von Deyn et al. [11] compared and contrasted the transition behavior of zero-pressure gradient boundary layer under the influence of surface roughness and free-stream turbulence (FST), employing DNS. The Reynolds number based on the roughness height (Re_k) was varied from 0 to 450 and the transition scenario were studied with and without FST. They found that in the absence of FST, the roughness-induced low-speed streaks undergo sinusoidal breakdown and develop secondary instabilities leading to the formation of turbulent boundary layer. Muppidi and Mahesh [12] conducted DNS of distributed roughness induced transition of a Mach 2.9 laminar boundary layer and distinguished the characteristics of streamwise vortices formed over distributed roughness with those around an isolated roughness element.

De Marchis et al. [13] conducted LES of channel flow simulations and correlated the roughness function (ΔU^+) of different surfaces with the corresponding characteristics such as the root-mean-square and equivalent sand grain roughness heights and effective slope. Their rough geometries were generated by the superimposition of sinusoidal functions with random amplitude values. Yang et al. [14] performed Direct Numerical Simulations of rough wall channel flows. In their work, pseudo-random roughness is generated mathematically using a random algorithm, wherein the power spectrum and probability density function of the surface height are prescribed as inputs. They compared their drag force predictions from their minimal channel simulations with the full-scale ones and discussed the sheltering effects of roughness scales. The Reynolds number dependence of the near-wall flow over real roughness mounted turbulent channels were investigated by Busse et al. [15] using DNS. Their results demonstrated that positively skewed (peak-dominated) rough surfaces lead to higher friction factors than negatively skewed (valley-dominated) ones. In another DNS based channel flow simulations by Jelly and Busse [16], roughness functions (ΔU^+) were quantified for three different Gaussian function based irregular surfaces with - peaks and pits, pits only and peaks only. It was found that the latter surface type is responsible for the main roughness effect, with the $\Delta U^+ = 5.9$ close to the peaks and pits surface ($\Delta U^+ = 6.8$) at $Re_\tau = 395$.

Downs III et al. [17] carried out hot-wire measurements of steady and unsteady boundary-layer disturbances, which are generated by quasi-random distributed roughness in an initially laminar boundary layer. They concluded that the transition downstream of 3D random roughness patterns is dictated by a competition between the unsteady-disturbance growth and stabilizing relaxation of the steady flow, and that this behavior is Reynolds number dependent. Direct Numerical Simulations of Sharma et al. [18] on discrete and quasi-random surface roughness show that disturbance generated by the tallest portions of roughness constructively or destructively interfere with each other and this affects the location of laminar to turbulent transition. Despite these advances, it remains unclear what characteristics of roughness are most important for transition, and why. As noted by Kadivar et al. [19] in their recent review paper, the impact of realistic roughness features on transition has received less attention. Accordingly, the objective of this study is to verify the effect of the finer scales of surface roughness on the transition onset using a series of high-fidelity, scale-resolving simulations. The transitional flow behavior of a laminar boundary layer is investigated under the influence of various realistic roughness patterns and at different inflow Reynolds numbers.

The outline of the paper is as follows. Firstly, the numerical framework is described providing the details of the flow domain, boundary conditions, real roughness geometries, test cases, spatial and temporal resolutions, and the in-house solver used to perform the simulations. In the next section, the instantaneous flow features including the large-scale and perturbation quantities are compared and contrasted among different test cases. In the subsequent sections, the effects of roughness scales and Reynolds number on the time-averaged flow field are investigated with the aid of turbulent kinetic energy and Reynolds stresses. Furthermore, a separate section dedicated on identifying the dominant features of the real roughness that affect the transition process is presented with the aid of additional scale-resolving simulations. Finally, concluding remarks and future recommendations are provided.

2 Numerical Methodology

2.1 Physical domain and boundary conditions

Figure 1(a) shows the schematic of the computational domain (and the boundary conditions) which corresponds to the widely investigated ERCOFTAC-T3A test case [20]. A Riemann inflow with a Blasius boundary layer is specified at the inlet. At the exit, a constant pressure outflow condition is imposed. To minimize acoustic reflections from the exit boundary, a streamwise grid stretching involving 40 points is employed [21]. Free-stream condition is applied at the top boundary and periodicity is imposed in the spanwise direction. Both the flat plate and the roughness patch over it are represented using the second order Boundary Data Immersion Method (BDIM), where the no-slip condition is satisfied using a meta equation [22, 23]. The inset plot shows the magnified view of the real roughness pattern. The meta equation when employed for a rough surface fixed in space takes the following form:

$$\Phi_\epsilon = f(\Phi, \vec{x}, t)\mu_0^{\epsilon,F} + \mu_1^{\epsilon,F}\frac{\partial}{\partial n}(f(\Phi, \vec{x}, t)) \tag{1}$$

where f is a generic notation representing all the three components of velocity and temperature and Φ_ϵ indicates the modified value of these primitive variables across the BDIM interface. n in Equation 1 indicates the direction of local normal to the rough surface. To ensure a smooth surface transition at the interface between smooth-to-rough and rough-to-smooth walls, a cosine function ramp [23, 24] is employed in line with our past studies. Figure 1(b) shows a portion of the roughness interface represented by the first and second-order BDIM weighting functions - $\mu_0^{\epsilon,F}$ and $\mu_1^{\epsilon,F}$, extracted at $x/\delta^*_{in} = 200$. These distributions mimic the topology of the real rough surface under consideration. These weighting functions are presented from the streamwise location with the smallest roughness wavelength ($32 < z/\delta^*_{in} < 34$). Since the grid spacing along the stream and spanwise directions are very nearly uniform in the roughness region, about 18 grid points are employed along each direction to resolve the roughness elements. The peak to peak roughness height is resolved by employing around 20 grid points. Figure 1(c) depicts the turbulent structures visualized using Q iso-surface which shows the real roughness induced transition of a laminar boundary layer.

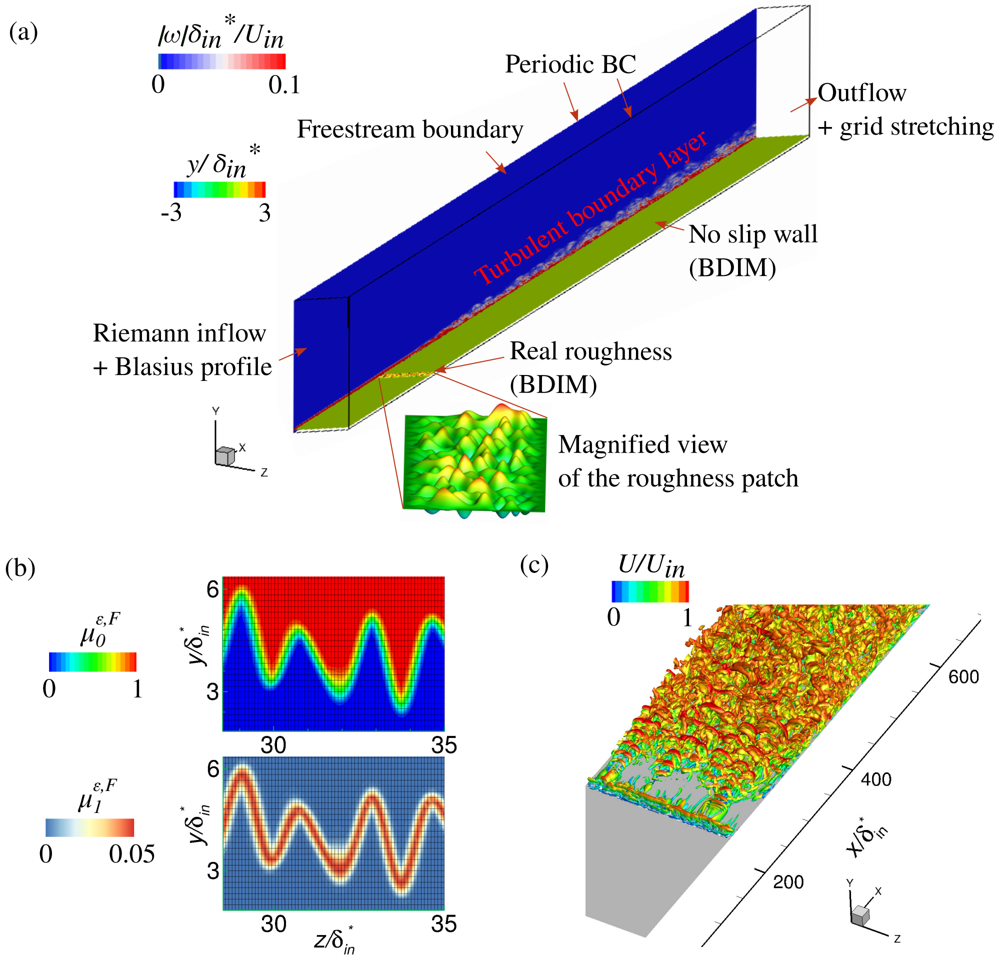

Fig. 1 (a) Computational domain and boundary conditions, (b) BDIM weighting distributions from $k_c = 15$ roughness - $\mu_0^{\epsilon,F}$, $\mu_1^{\epsilon,F}$ and (c) Vortical structures visualized using Q iso-surfaces (Q=0.0005) and coloured with streamwise velocity.

A highly irregular surface topology is generated by employing the MARS (Multi-scale Anisotropic Rough Surface) algorithm of Jelly and Busse [25], which creates a two-dimensional double periodic surface based on a linear combination of Gaussian random number matrices. This algorithm can generate roughness patches for any given streamwise and spanwise extent thereby avoiding the need to repeat/mirror a rough patch. The rough patch is placed between $190 < x/\delta^*_{in} < 210$. Accordingly, the streamwise extent of the rough surface is given by $L_x \approx 20\delta^*_{in}$. Surfaces with different roughness wavelengths are generated from the same underlying roughness pattern by employing a low-pass filter with different cut-off values, k_c. Figures 2(a) and (b) show the contours of the roughness topologies with the cut-off filter values of $k_c = 7$

and $k_c = 15$, respectively. Note that these surfaces are obtained by applying different cut-off filters on the same underlying surface, implying that both these surfaces have similar features at each location. The corresponding power spectral densities are also shown as an inset plot in each figure. In the insets, the x and y axes denote the streamwise and spanwise wavenumber of the roughness topology with respect to the flow direction. It is clear that the roughness scales (specifically the roughness wavelength) can be controlled by varying the value of k_c, with a larger value accommodating finer roughness features. For example, it is evident from the roughness patterns that $k_c = 15$ incorporates finer scales of roughness when compared to $k_c = 7$. The objective of this study is to verify the effect of these finer scales on the transition onset. For the $k_c = 7$ surface, the tallest scales (the circled region in Figure 2(a), for instance) govern the transition process as will be seen shortly.

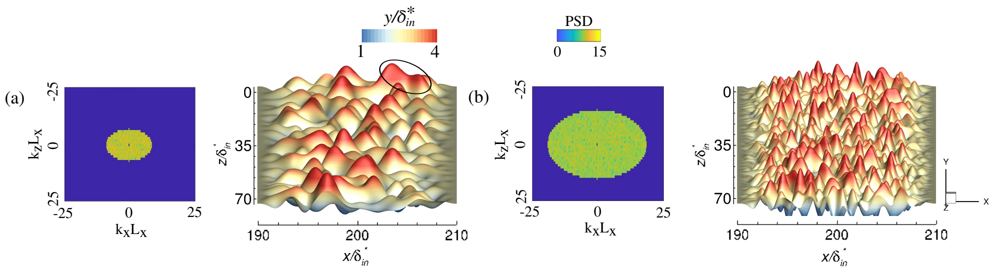

Fig. 2 Isometric view showing the real roughness patches coloured with the local roughness height for (a) $k_c = 7$ and (b) $k_c = 15$. The corresponding Power Spectral Densities are also shown. L_x refers to streamwise extent of the rough surface.

For both these surfaces, Table 1 lists the maximum peak to valley height (R_z), root-mean-square height (k_{rms}), skewness (Sk), and kurtosis (Ku) of the roughness patch. The length scales R_z and k_{rms} are normalized by δ^*_{in} and the cut-off wavenumber k_c is normalised by the inverse of δ^*_{in}. As evident from the table, the roughness parameters R_z, k_{rms}, and Ku are similar for both the surfaces. However, the skewness for $k_c = 7$ is positive while that of $k_c = 15$ is negative. It indicates that $k_c = 15$ surface has more valleys (than peaks) when compared to $k_c = 7$ surface. Simulations are performed at Reynolds numbers 540 and 360, defined in terms of the displacement thickness at the inlet, δ^*_{in}, and inlet velocity, U_{in}. These correspond to a Re_{krms} of ≈ 452 and ≈ 302 respectively based on the r.m.s height, k_{rms}, of the roughness elements. It is worth mentioning that the current study is motivated by how turbine/compressor blades degrade in a gas turbine engine. With time, the blades progressively degrade due to an increase in the roughness scales. Test cases with $k_c = 7$ and $k_c = 15$ typically replicate this scenario. Also, the blades encounter different Reynolds numbers during take-off and cruise thereby altering the transition on a given rough surface. Test cases with $Re = 360$ and $Re = 540$ replicate this scenario. For all the test cases presented in Table 3 an initial solution based on kc15Re540 is used to start the computations and no specific initialization was employed for kc15Re540.

In addition to the aforementioned cases, a third surface with $k_c = 3$ filter investigated is a valley-dominated one with relatively large mean-square roughness height. Since the roughness statistics for this surface are significantly different from the other two surfaces, the majority of the discussion will focus on $k_c = 7$ and $k_c = 15$ surfaces thereby discussing only the key aspects of transition from the $k_c = 3$ surface. Furthermore, additional test cases are investigated, based on the selective retention of roughness features the information of which is provided in section 3.3.

Table 1 Details of the test cases

Acronym	Roughness filter (k_c)	Reynolds number ($Re_{\delta^*_{in}}$)	R_z	k_{rms}	Sk	Ku
kc15Re540	15	540	6.67	0.838	-0.084	2.972
kc15Re360	15	360	6.67	0.838	-0.084	2.972
kc7Re540	7	540	5.9	0.830	0.082	2.976
kc7Re360	7	360	5.9	0.830	0.082	2.976
kc3Re540	3	540	6.23	1.14	-0.128	2.616
kc3Re360	3	360	6.23	1.14	-0.128	2.616

2.2 Solver details and simulation parameters

A high-order structured multi-block in-house solver, COMPSQUARE, is employed to solve the 3D compressible Navier–Stokes equations in generalized curvilinear coordinates [6]. In the current simulations, all the spatial derivatives are computed using 4^{th} order explicit schemes, and an 8^{th} order implicit filter with a filter coefficient of α_f = 0.48 is employed to suppress high-frequency dispersion errors. Visbal and Gaitonde [26] demonstrated the superior performance of a compact filter compared to sub-grid scale models. Hence all the simulations in this work are performed on a fine mesh using the compact filter without any explicit sub-grid scale models. An explicit 4-stage 4^{th} order Runge-Kutta scheme is used for time integration. For $Re_{\delta^*_{in}} = 540$, the Reynolds number in the computational domain varies between $1.0 \times 10^5 \leq Re_x \leq 11.2 \times 10^5$. The coherent structures are resolved on a grid comprising approximately 83 million grid points with a time step of 0.045 δ^*_{in}/U_{in}, which corresponds to $CFL \approx 1$. It is worth noting that the spanwise domain width in the present test cases are chosen based on the transitional boundary layer investigation of Pinto and Lodato [20]. Since the focus of this paper is strictly on transition, the current domain width is smaller than that employed in the LES of turbulent boundary layer simulations by Schlatter et al [27]. Table 2 lists the key input parameters of the computational domain and grid. As the majority of discussions in this paper will be focusing on $Re_{\delta^*_{in}} = 360$, the grid resolution reported are based on this Reynolds number. Since the compressible Ma of 0.5 is typical of transitional boundary layers in turbine flows, the same value has been retained in the current investigation of transition. The grid size presented in this table excludes the additional grid count of 40 streamwise points from the stretched part (non-physical) of the domain, mentioned in the subsection 2.1. The viscous grid spacings provided are based on the averaged value of skin-friction velocity ($u_{\tau_{av}}$) in the turbulent regime of the boundary layer.

Table 2 Simulation and grid parameters

Parameter	Variable	Value
Reynolds number based on δ^*_{in} and U_{in}	$Re_{\delta^*_{in}}$	360, 540
Mach number	Ma	0.5
Domain dimensions	$L_{x1} \times L_y \times L_z$	$1912\delta^*_{in} \times 214\delta^*_{in} \times 70.2\delta^*_{in}$
Domain dimensions for extended span	$L_{x1} \times L_y \times L_z$	$1912\delta^*_{in} \times 214\delta^*_{in} \times 140.4\delta^*_{in}$
Number of grid points in the domain	$N_x \times N_y \times N_z$	$925 \times 120 \times 721$
Streamwise grid spacing based on $u_{\tau_{av}}$	$\Delta x^+_{min}, \Delta x^+_{max}$	1.75, 30.64
Near-wall grid spacing based on $u_{\tau_{av}}$	$\Delta y^+_w, \Delta y^+_{max}$	1, 21
Spanwise grid spacing based on $u_{\tau_{av}}$	Δz^+	1.66

The computational domain of $965 \times 120 \times 721$ grid points is decomposed into three blocks of approximately equal size, and one Graphics Processing Unit (GPU) each is assigned to these three blocks. Following Gaitonde and Visbal [28], we employ a six-point overlap between the block interfaces to preserve the accuracy of the numerical scheme. For the simulations, three A100 GPUs with 40 GB are employed and the communication between them is facilitated through the message passing interface (MPI).

3 Results and discussion

Firstly, the adequacy of the spanwise resolution of the roughness features is established by performing a grid sensitivity study employing $N_z = 361$ and 721 points for the $k_c = 7$ rough surface for both the Reynolds numbers. Figure 3(a) shows the wall-normal variation of the streamwise Reynolds stress at four different streamwise locations in the form of a carpet plot. Figure 3(b) compares the streamwise variation of the maximum velocity perturbations for these cases, respectively. It is clear that grid independent results are achieved beyond a resolution of $N_z = 361$. However, all the test cases discussed in this paper are carried out employing $N_z = 721$ spanwise points.

Subsequently, the sensitivity to the time averaging duration is examined with respect to the $k_c = 7$ surface at $Re_{\delta^*_{in}}$ of 540. The initial transients are flushed out for two throughflows (a through flow, TF, is a characteristic time scale defined based on the free-stream velocity and the streamwise extent of the domain) following the recommendation of Wenzel et al. [29] before commencing the time averaging. Figures 3(c) and (d) compare the streamwise evolution of the momentum thickness and streamwise velocity perturbations for different averaging duration. It is evident that the first and second order statistics have all converged after five through flows of averaging and any further averaging has a negligible effect. Accordingly, all the results presented in the paper are based on five through flows of averaging duration.

The adequacy of the spanwise extent of the domain is established by comparing the transition onset behaviour of the kc7Re360 case from Table 1 for $L_z = 70.2\delta^*_{in}$ and $140.4\delta^*_{in}$ (see also Table 2). Figures 4(a) and (b) compare the instantaneous flow features in the transition region for these two test cases using Q iso-surfaces. For the $L_z = 140.4\delta^*_{in}$ case, the roughness patch from the kc7Re360 case with $L_z = 70.2\delta^*_{in}$ is duplicated seamlessly along the span such that the same roughness features are

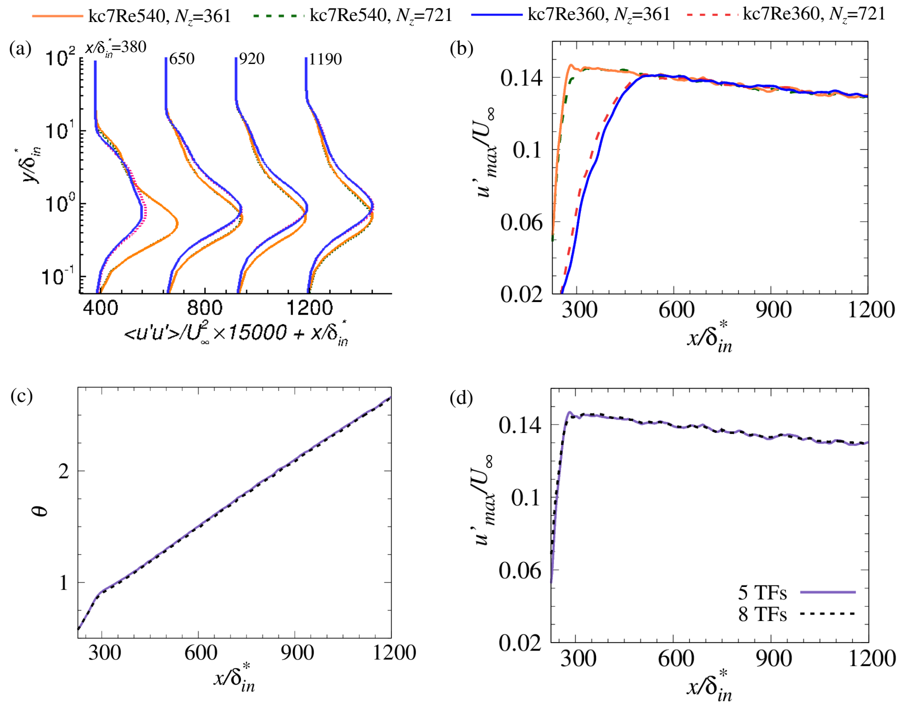

Fig. 3 Sensitivity of the $k_c = 7$ roughness to the spanwise grid resolution for $Re_{\delta^*_{in}} = 540$ and 360: (a) wall-normal variation of Reynolds normal stress at different streamwise locations and (b) variation of streamwise velocity perturbations. Convergence of the kc7Re540 case with respect to the time averaging duration: streamwise variation of (c) momentum thickness and (d) maximum streamwise velocity perturbations.

encountered between any two points in the spanwise direction separated by $L_z = 70.2\delta^*_{in}$. It is evident that the transition onset for the extended domain exhibits a consistent behaviour with that of the kc7Re360 case with $L_z = 70.2\delta^*_{in}$. Furthermore, Figures 4(c) and (d) show the spanwise auto-correlation coefficients from two different streamwise locations, $x/\delta^*_{in} = 430$ and 600, respectively, based on $L_z = 70.2\delta^*_{in}$. The correlation coefficient is computed using the equation:

$$R_{uu}(z) = \frac{< u'(x,y,z,t)u'(x,y,z+\Delta z,t) >}{< u'(x,y,z,t)u'(x,y,z,t) >} \tag{2}$$

where Δz is the spanwise lag and the operator $< \cdot >$ represents time averaging. u' at every time instant is computed as $u(x,y,z,t) - \overline{u}(x,y,t)$. At both the streamwise locations the correlation coefficients starts from unity at $z/\delta^*_{in} = 0$ and undergo multiple zero crossings at different spanwise locations. The coefficients progressively decays with spanwise lag and tends to zero close to the mid span of the domain ($z/\delta^*_{in} \approx 35$) thereby ensuring the de-correlation of the signal within the chosen spanwise extent. This demonstrates that a computational domain with $L_z = 70.2\delta^*_{in}$ is sufficient enough to capture all the vortical structures of the flow field and hence this spanwise extent has been retained for all the test cases presented in this paper.

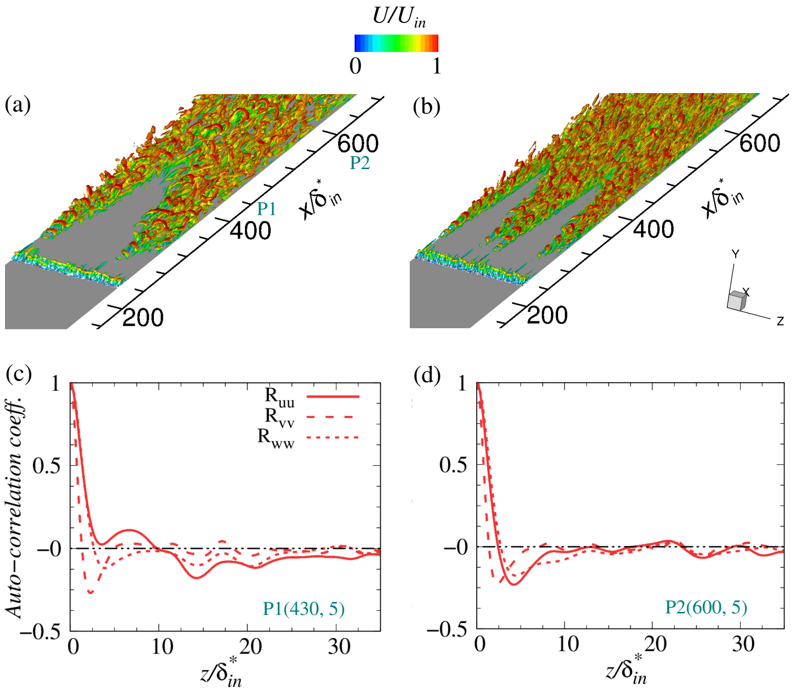

Fig. 4 Visualization of flow structures using Q iso-surfaces (Q=0.001) for the case kc7Re360. The structures are coloured with streamwise velocity (a) $L_z = 70.2\delta^*_{in}$ and (b) $L_z = 140.4\delta^*_{in}$. (c, d) Spanwise auto-correlation coefficient from $L_z = 70.2\delta^*_{in}$ at two different streamwise locations close to the wall.

Secondly, the high-fidelity numerical simulation set-up is validated against the data available in the literature. Towards this, the NV test case (kc7 surface without valleys at $Re_{\delta^*_{in}} = 360$, to be discussed in section 3.3) is chosen. Figure 5(a) compares the near-wall velocity profiles in viscous units for $Re_\theta = 1006$ (extracted at $x = 1200\delta^*_{in}$) against the KTH DNS 2012 data base of Schlatter et al. [27, 30]. A good agreement against the reference data is achieved for the Re_θ values compared. Figure 5(b) further compares the wall-normal variation of the Reynolds normal stresses with the reference DNS data. A favorable agreement is obtained for most portions of the turbulent boundary layer with subtle discrepancies observable close to the outer turbulent boundary layer. This could be attributable to marginally lower grid resolution in this region. Since the present paper focuses on the transitional behaviour of the boundary layer very close to the wall at a much upstream streamwise extent, the transitional effects due to the roughness features occur within the well resolved region and hence the current grid resolution is deemed sufficient enough.

In the following subsections, we present the various instantaneous and time averaged flow features in detail for all the test cases investigated.

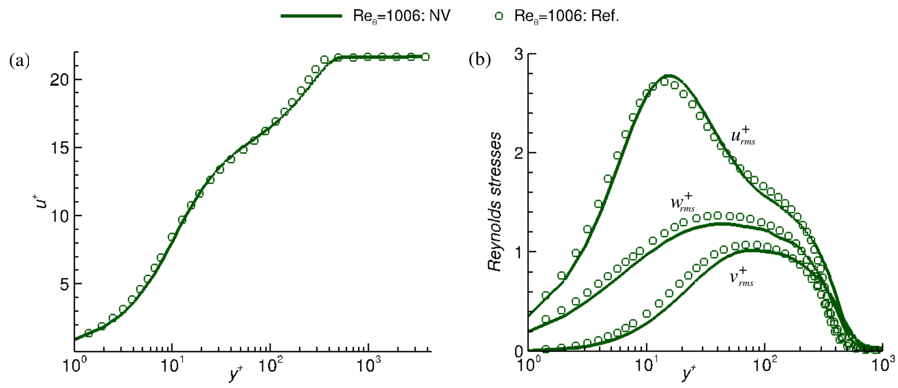

Fig. 5 Comparison of (a) near-wall mean velocity profiles and (b) Reynolds stresses, from the NV test case with the Direct Numerical Simulations from the KTH data base [30] at $Re_\theta = 1006$.

3.1 Instantaneous flow features

For all the cases, Figures 6(a-f) compare the evolution of transitional vortical structures using Q iso-surfaces of the instantaneous flow field. The structures are colored using streamwise velocity. The roughness patch for each case is also shown in the background. A comparison of these cases reveals that a higher Reynolds number shortens the transition length, as evidenced by the upstream shift in the turbulent breakdown at $Re_{\delta^*_{in}} = 540$ compared to the $Re_{\delta^*_{in}} = 360$ (see the circled regions). Also at the high Reynolds number a comparison of Figures 6(a) and (b) shows that the density of the hairpin vortices generated by $k_c = 15$ roughness appears to be higher compared to both the $k_c = 7$ and $k_c = 3$ surfaces (refer again to the circled regions). This effect could possibly be attributed to the higher frequency content of the $k_c = 15$ roughness. At both Reynolds numbers, the streamwise location at which the hairpin structures first appear varies across the span. This reflects the spanwise non-homogeneity of the roughness and the sensitivity of transition behavior to the local roughness scales and features. This behavior is more evident from Figures 6(d-f) at $Re_{\delta^*_{in}} = 360$ where the $k_c = 15, 7$ and 3 roughnesses lead to the development of distinct transition onset boundaries (roughly marked in the figures). For the kc15Re360 case, an approximate wedge-shaped transition onset boundary, which is almost symmetric about the mid-span of the domain develops. For $k_c = 7$ roughness pattern, the hairpin vortices are shed immediately downstream but close to one of the periodic boundaries for both the Reynolds numbers, $Re_{\delta^*_{in}} = 540$ and 360. The corresponding roughness feature that is responsible for the shedding of these vortices is shown as an inset plot in Figure 6(b). Clearly, the presence of this streamwise elongated hump-like roughness feature leads to an early onset of vortex shedding. This roughness feature, which is also prominent in Figure 2(a), further elucidates the sensitivity of transition behavior to roughness scales that differ along the span. The influence of such features becomes even more prominent for the kc3Re360 case. The inset associated with Figure 6(c) shows the magnified view of one of the major roughness peaks dictating the transition onset at both $Re_{\delta^*_{in}} = 540$ and 360 for the $k_c = 3$ roughness.

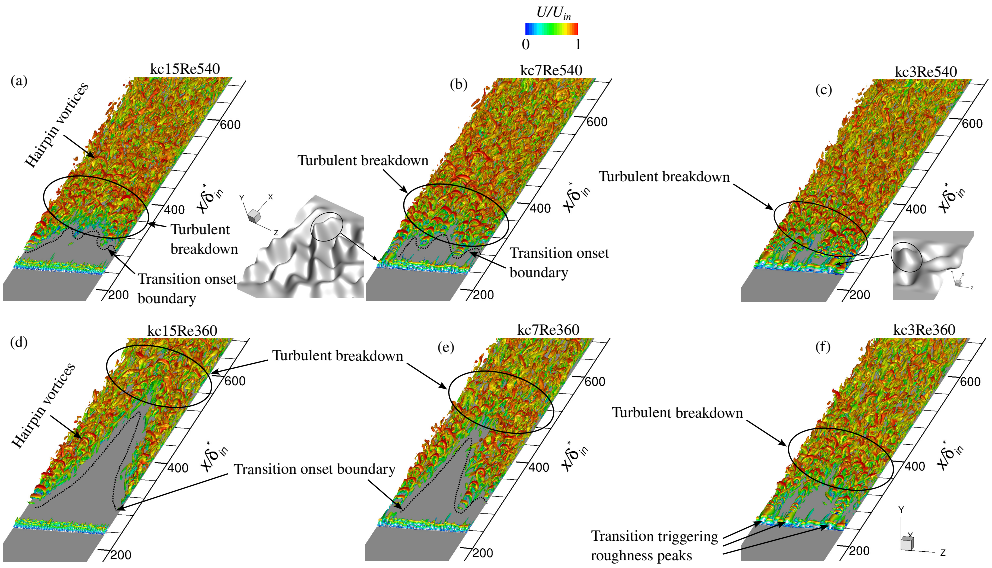

Fig. 6 Visualization of flow structures using Q iso-surfaces (Q=0.001). The structures are coloured with streamwise velocity.

Figure 7(a) compares the instantaneous contours of wall-normal vorticity extracted close to the wall. For each case, the cross-section of the corresponding roughness patch is also shown in the background ($x/\delta^*_{in} \approx 200$). As expected, for a given rough surface, the transition extent increases with a decrease in the Reynolds number (see the cases kc15Re540 and kc15Re360). For a given Reynolds number, note that the strength of steady streaks behind the roughness patch increases with a decrease in the value of k_c. This is attributed to the fact that the roughness peaks and valleys are relatively sparsely packed for $k_c = 7$ compared to $k_c = 15$ (see also Figures 2(a) and (b)). The reduced sheltering effect between the sparse roughness elements (Yang et al. [31]) facilitates the development of stronger vortices around the remaining roughness protrusions. Figure 7(b) further examines the effects of Reynolds number on the transition onset for the cases kc15Re360 and kc7Re540 with the aid of space-time (ST) plots of the instantaneous skin-friction coefficient (C_f), computed using Equation 3. The simulations for the cases, kc15Re360, kc7Re540, and kc7Re360, were initialized using the flow field of kc15Re540. This exercise enabled us to examine the time required for the flow to adjust to the new transition onset location with varying Reynolds number and frequency content of the roughness. For example, the ST plot of kc15Re360 shows higher C_f during the initial transients before the new location of transition onset is established. For all the test cases examined, we observe that the new transition onset location is established very quickly within $\approx 1725 k_{rms}/U_{in}$ when the simulations are initialized with the flow field of kc15Re540. In contrast, when initialized from scratch, the simulations have to be carried out for a non-dimensional time of $\approx 4600 k_{rms}/U_{in}$ for the flow to achieve a statistically steady state. The ST plot for the kc15Re360 case shows a clear delay in the onset of turbulence after the

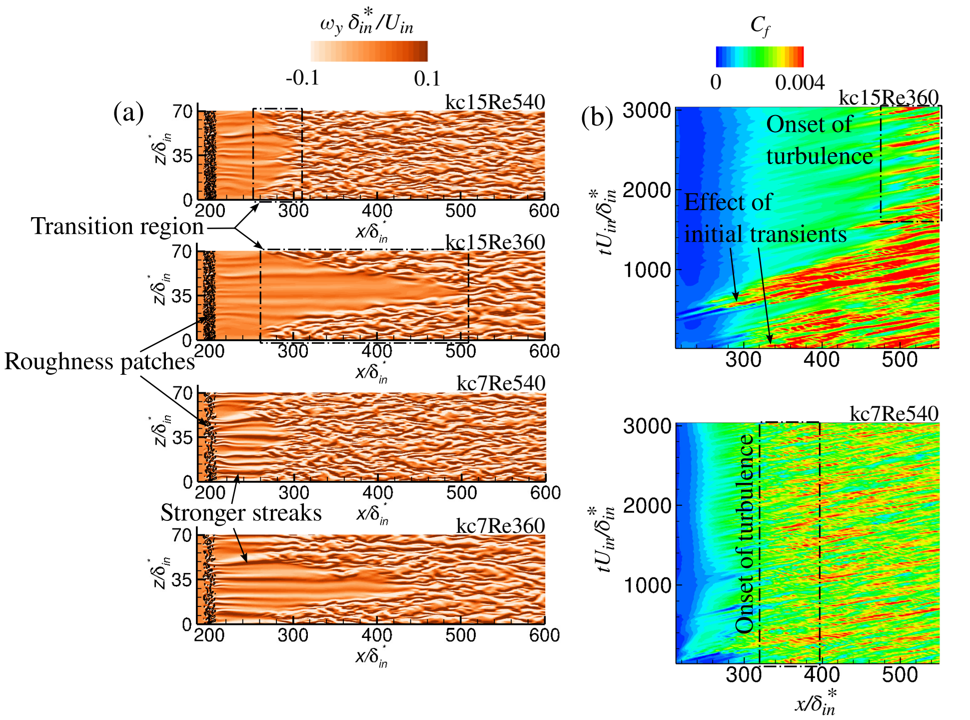

Fig. 7 (a) Instantaneous contours of wall-normal vorticity at a location very close to the wall ($\frac{y}{\delta} \approx 8\%$ where δ is measured at $x/\delta^*_{in} = 200$) and (b) space-time plots of C_f from mid-span of the domain.

initial transients are flushed out. However, for the kc7Re540 case, there is no noticeable delay in the transition onset as the effect of changing the roughness pattern seems to have little impact at a higher Reynolds number.

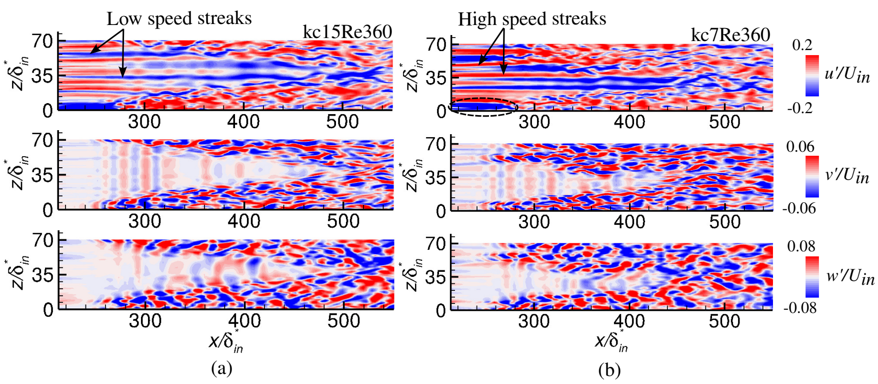

Fig. 8 Wall-normal contours of instantaneous velocity perturbations in the transitional regime. Contours are extracted at $y \approx \delta/2$ where δ is measured at $x/\delta^*_{in} = 200$.

Figure 8(a) and (b) show the streamwise evolution of perturbation velocities in the transitional regime for the cases kc15Re360 and kc7Re360 cases, respectively. These contours are obtained by subtracting the instantaneous flow field from the corresponding span-averaged data. The contours of u' perturbations clearly show the low-speed (negative u') and high-speed (positive u') streaks. The steady streaks behind the $k_c = 7$ surface are visibly stronger than those behind the $k_c = 15$ surface. As discussed before, this is attributed to the reduced sheltering effect by the finer roughness scales. For the kc7Re360 case, the thick low-speed streak between $215 < x/\delta_{in}^* < 280$ close to $z/\delta_{in}^* = 0$ (circled in Figure 8(b)) is generated behind the hump-like roughness scale discussed in Figures 6(b) and 2(a). The streamwise (u') and wall-normal (v') fluctuations are symmetric about the centreline of the streak, and the spanwise (w') velocity fluctuations are found to be anti-symmetric. These mode shapes are reminiscent of the varicose instabilities reported by Hack and Zaki [32], implying that the streak instability in the current simulations is triggered due to the varicose modes.

3.2 Turbulent statistics

Figure 9(a) compares the streamwise evolution of the time and span-averaged skin friction coefficient, C_f for all the cases. The skin-friction coefficient is computed using the following relations:

$$\tau_w = \frac{\mu_{av}}{Re_{\delta_{in}^*}} \frac{\partial U_{av}}{\partial n} \qquad C_{f_{xr}} = \frac{\tau_w}{\frac{1}{2}\rho_e U_e^2} \qquad C_f = \frac{1}{L_z}\int_0^{L_z} C_{f_{xr}} dr \tag{3}$$

where τ_w denotes the shear stress. μ_{av}, U_{av}, ρ_e and U_e denote the time-averaged values of dynamic viscosity, streamwise velocity, free-stream density, and free-stream velocity, respectively. $C_{f_{xr}}$ denotes the time-averaged skin-friction coefficient over the rough surface with r representing the spanwise running coordinate along the roughness. L_z indicates the spanwise extent of the computational domain.

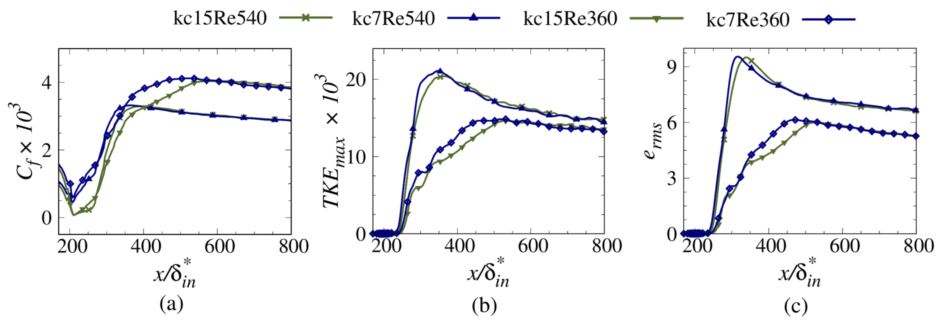

Fig. 9 Streamwise evolution of various statistical quantities for all the cases. (a) Time and span averaged C_f, (b) time and span averaged maximum turbulent kinetic energy and (c) disturbance energy for all the cases in the transitional regime. For a better representation, every 25 data points are skipped in each curve.

Figure 9(b) also plots the streamwise variation of the maximum turbulent kinetic energy (TKE_{max}). To generate this plot, the peak TKE in the wall-normal direction is determined at every streamwise and spanwise location and are subsequently span-averaged to obtain a streamwise varying TKE_{max}. The onset of transition and turbulence can be defined as the streamwise locations where the C_f acquires the minimum and maximum values, respectively [33]. Both rough surfaces show a similar variation in skin-friction coefficient for a given Reynolds number, with marginal differences in the transitional region ($200 \leq x/\delta^*_{in} \leq 350$ for $Re_{\delta^*_{in}} = 540$ and $200 \leq x/\delta^*_{in} \leq 600$ for $Re_{\delta^*_{in}} = 360$). From the C_f curves, it is evident that the turbulent onset occurs at $x/\delta^*_{in} \approx 350$ for $Re_{\delta^*_{in}} = 540$ and at $x/\delta^*_{in} \approx 500$ for $Re_{\delta^*_{in}} = 360$ thus implying an increase in the transition length with a decrease in the Reynolds number. This behavior is consistent with the appearance of hairpin structures in the Q iso-surfaces discussed earlier. As expected, the location of the transition onset and the peak value of the TKE_{max} are also identical for both rough surfaces. It affirms that, for the Reynolds number considered in the current simulations, higher roughness frequencies have a negligible effect on the transition onset. However, it is interesting to note that for a given Reynolds number, there appears to be a marginal decrease in the transition length for $k_c = 7$ compared to the $k_c = 15$ surface. This could possibly be due to the stronger streaks and enhanced mixing in the presence of sparsely packed roughness features ($k_c = 7$) which promote earlier turbulent breakdown. Both the peak TKE_{max} and its growth rate is significantly higher for $Re_{\delta^*_{in}} = 540$ cases compared to the $Re_{\delta^*_{in}} = 360$ cases. A monotonic increase in the TKE_{max} is observable for the $Re_{\delta^*_{in}} = 540$ case. This is in contrast to the $Re_{\delta^*_{in}} = 360$ case where an initial rapid rise in the TKE_{max} from $200 \leq x/\delta^*_{in} \leq 350$ is followed by a more gradual rise from $350 \leq x/\delta^*_{in} \leq 600$. A similar trend is observed in Figure 9(c), which depicts the streamwise evolution of the total disturbance energy [34] associated with the velocity fluctuations, $u^{'}_{rms}$. Here $u^{'}_{rms}$ is defined as the $\sqrt{< u'u' >}$, where $< \cdot >$ denotes time-averaging. The total disturbance energy is computed based on the time-averaged streamwise velocity fluctuations using the expression below:

$$e_{rms} = \int_{\eta=0}^{\eta=\infty} \int_{z=0}^{z=L_z} [u^{'}_{rms}(x, y, z)]^2 dz d\eta \tag{4}$$

where z is the spanwise coordinate and η is the wall-normal Blasius coordinate normalised by the boundary layer length scale, δ [34]. Equation 4 states that the streamwise evolution of the disturbance energy could be tracked by integrating the square of the velocity perturbations over the entire boundary layer in wall-normal and spanwise directions at every streamwise location.

For all the cases investigated, Figures 10(a-d) compare the turbulent kinetic energy contours on a wall-parallel plane, $y \approx 8\%\delta$. Here δ corresponds to the boundary layer edge at $x/\delta^*_{in} \approx 200$. The spanwise pattern of the turbulent breakdown resembles the transition onset pattern discussed in conjunction with the Q iso-surfaces in Figures 6(a-d). At $Re_{\delta^*_{in}} = 540$, the turbulent breakdown occurs between $280 < x/\delta^*_{in} < 380$, as indicated by the enhanced TKE generation in this region. Although the overall transitional behavior at $Re_{\delta^*_{in}} = 540$ is similar for $k_c = 15$ and $k_c = 7$ surfaces, the spanwise variation of the turbulent breakdown appears to be sensitive to the frequency

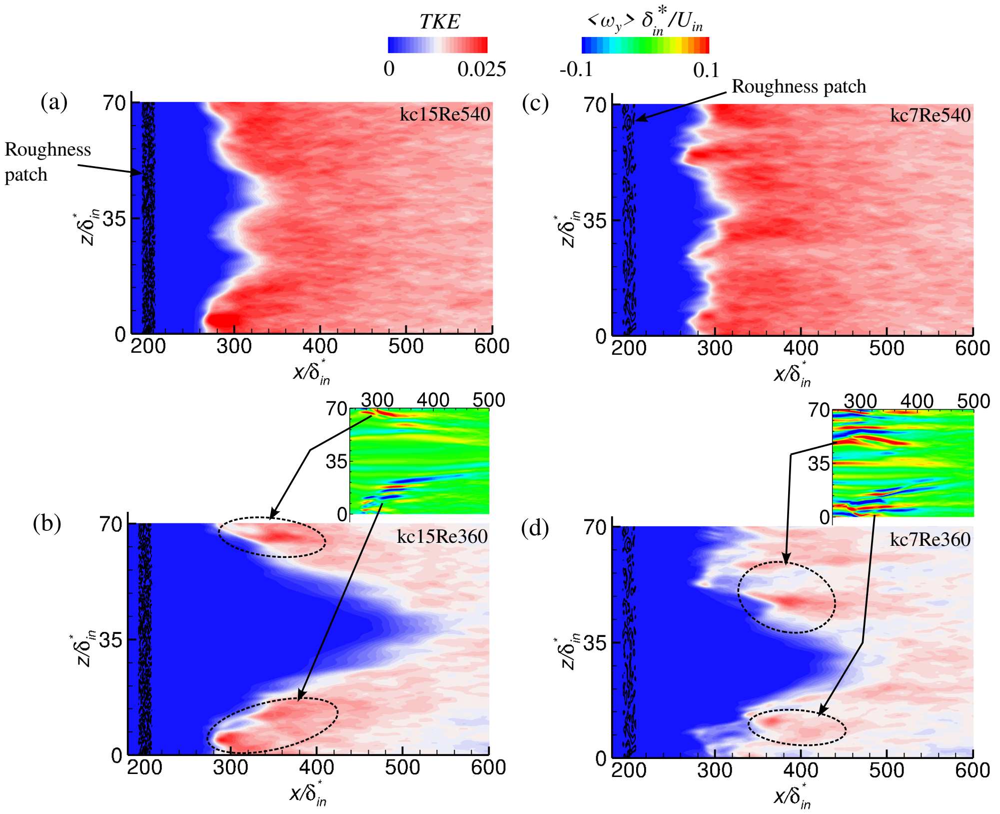

Fig. 10 Turbulent kinetic energy contours at a wall-normal location of $\frac{y}{\delta} \approx 8\%$ (where δ is measured at $x/\delta^*_{in} = 200$). The corresponding wall-normal vorticity is also shown as an inset plot for the cases kc15Re360 and kc7Re360.

of the roughness scales. For both Reynolds numbers, the distribution of TKE is much more homogeneous in the span in the absence of high roughness wavenumbers ($k_c = 7$) due to enhanced three-dimensional mixing. Localised spots of enhanced TKE (marked with circles) are also evident in Figures 10(b) and (d) within the transition region. Such regions are characterised by high wall-normal vorticities as shown in the inset plot corresponding to each case. We will now explore the individual features of the rough surfaces in more detail.

Figures 11(a-d) show the streamwise and spanwise distributions of the time-averaged skin-friction coefficient for different test cases. For each case, a magnified view of the distribution over the roughness pattern is also presented. Figures 11(a-d) show that the onset of turbulence occurs at $x/\delta^*_{in} \approx 300$ for $Re_{\delta^*_{in}} = 540$ and at $x/\delta^*_{in} \approx 550$ for $Re_{\delta^*_{in}} = 360$ which are consistent with the observations in Figure 9(a). Patches of enhanced shear (marked in the Figures 11(c) and (d)) are observable behind the $k_c = 7$ surface at both the Reynolds numbers. The sparsely packed roughness features in $k_c = 7$ case facilitate the formation of horseshoe vortices which

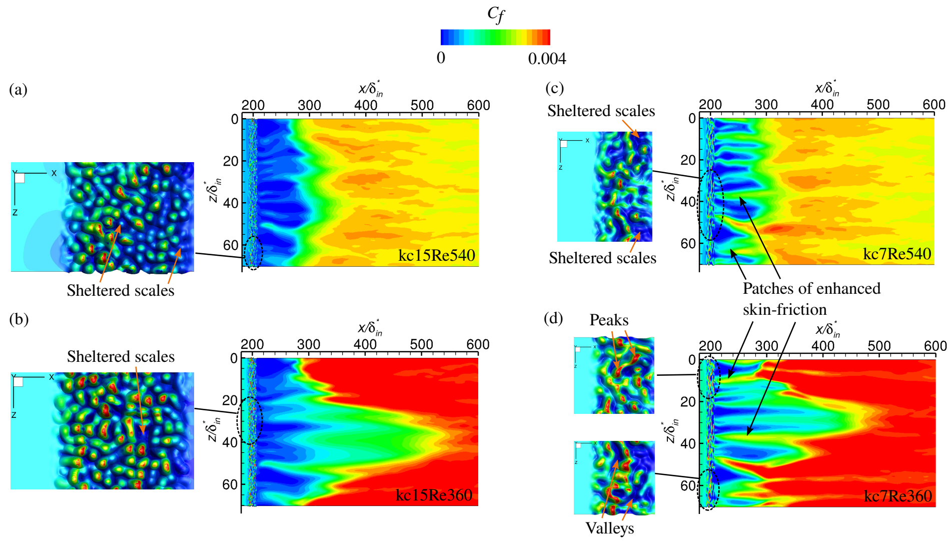

Fig. 11 Contours of skin-friction coefficient (C_f) in the transitional regime for the different cases. Insets show the distribution of C_f over the roughness patch.

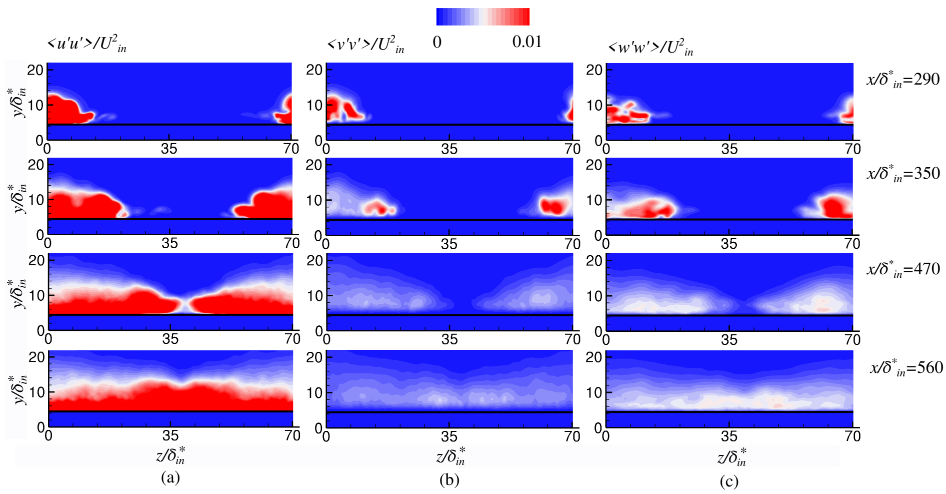

Fig. 12 Cross-plane contours of Reynolds stresses in the transitional regime for the kc15Re360 case. (a) Streamwise, (b) wall-normal, and (c) cross-stream stresses

wrap around the roughness elements thereby causing stronger streaks to develop in the transition region (see the cases kc7Re540 and kc7Re360 in Figure 7(a)). This in turn increases the spanwise homogeneity of the flow in the transition region. However, for $k_c = 15$ case, the roughness features are much more closely packed which constrains the development of horseshoe vortices around the roughness elements. As a result, the reduced spacing between the roughness scales causes the unstable shear layers to predominantly separate from the tip of the elements. Similar observations are reported by the eddy-resolving simulations of Ganesh et al. [35] who explored the effect of spacing between the distributed roughness elements on open cavity flows. In all four cases, the magnified views of skin-friction distribution over the roughness patch indicate that the peaks are exposed to intense flow shear, and the valleys experience the lowest skin friction. This suggests the existence of local pockets of reverse flow in the valleys. The skin-friction distribution over the roughness patch for different cases further reveals the sheltering due to taller roughness scales [31]. This is identifiable from the regions of lower shear over the smaller roughness peaks that are located on the leeward side of taller peaks (marked in Figures 11(a-c)).

For the kc15Re360 case, Figures 12(a-c) further compare the evolution of the different Reynolds stress components over the cross-flow planes extracted at four different streamwise locations in the transitional region. The signature of wedge-shaped transition onset is evident in all three components of the Reynolds normal stresses. The transition is triggered close to the periodic boundaries as evident from the Reynolds stress contours at $x/\delta^*_{in} = 290$. This is attributed to the fact that the dominant roughness feature triggering the transition process is located close to the periodic boundaries as demonstrated in Appendix A. As could be seen from the cross-flow planes $350 \leq x/\delta^*_{in} \leq 560$, the turbulent wedge progressively spreads towards the mid-span of the domain with streamwise distance. The Reynolds normal stress in the streamwise direction ($< u'u' >$) is the dominant contributor to the turbulent kinetic energy. Although the lateral ($< w'w' >$) and wall-normal stresses ($< v'v' >$) are strongest immediately downstream of the roughness, they progressively decay with the streamwise distance.

3.3 Selective retention of roughness features

The results presented thus far show the effects of frequency filtering of the roughness on the boundary layer transition. The detailed flow around roughness elements shown in the inset plots of Figure 11 also highlights the importance of individual features and their interaction with the flow. In this section, we therefore examine spatial filtering of the $k_c = 7$ roughness to help identify the dominant roughness features affecting the transition process. For this investigation, the $k_c = 7$ surface is retained as the baseline from which other surfaces are derived through a systematic numerical procedure, to be discussed shortly. Table 3 shows the test case details of three additional scale-resolving simulations performed based on different derived rough surfaces.

Table 3 Test cases based on $k_c = 7$ and $Re_{\delta^*_{in}} = 360$

Acronym	Description	R_z	k_{rms}	Sk	Ku
NV	No Valleys	3.0	0.493	2.265	8.468
NV10P	No Valleys and top 10 Peaks	3.0	0.350	4.467	24.123
NV20P	No Valleys and top 20 Peaks	3.0	0.420	3.287	14.064

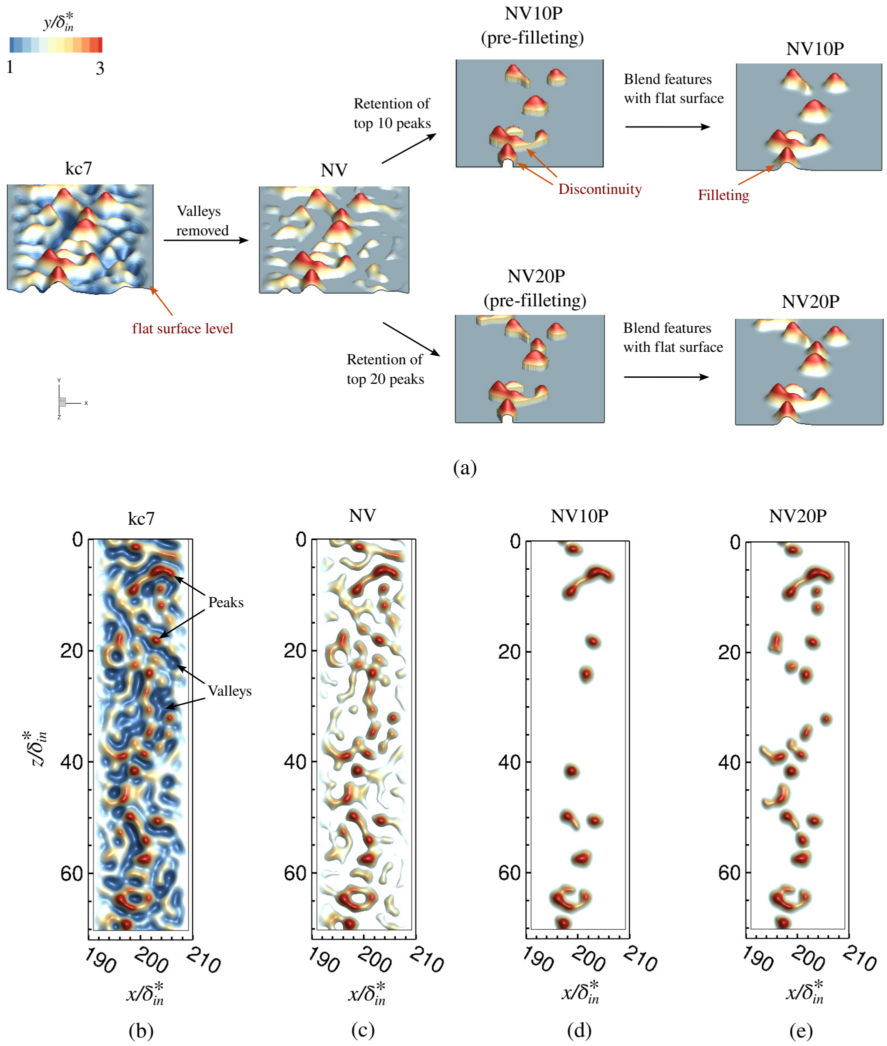

Fig. 13 (a) Numerical procedure showing the selective retention of dominant roughness features from $k_c = 7$ rough surface. Top view of different rough surfaces employed for simulations: (b) kc7, (c) NV, (d) NV10P and (e) NV20P.

Figure 13(a) shows the numerical steps involved in generating the new rough surfaces - NV, NV10P, and NV20P from the kc7 surface using codes written in MATLAB. The NV roughness, which is devoid of any valleys is generated from the kc7 surface by simply elevating the valley locations to the flat surface level (marked in Figure 13(a)). The other two surfaces are generated from the resulting NV roughness following a two-step process: (1) To isolate the effects of the largest peaks an appropriate cut-off height above the flat surface level is chosen, based on a certain fraction of the maximum peak height, such that only a required number of tallest peaks are retained. These numbers

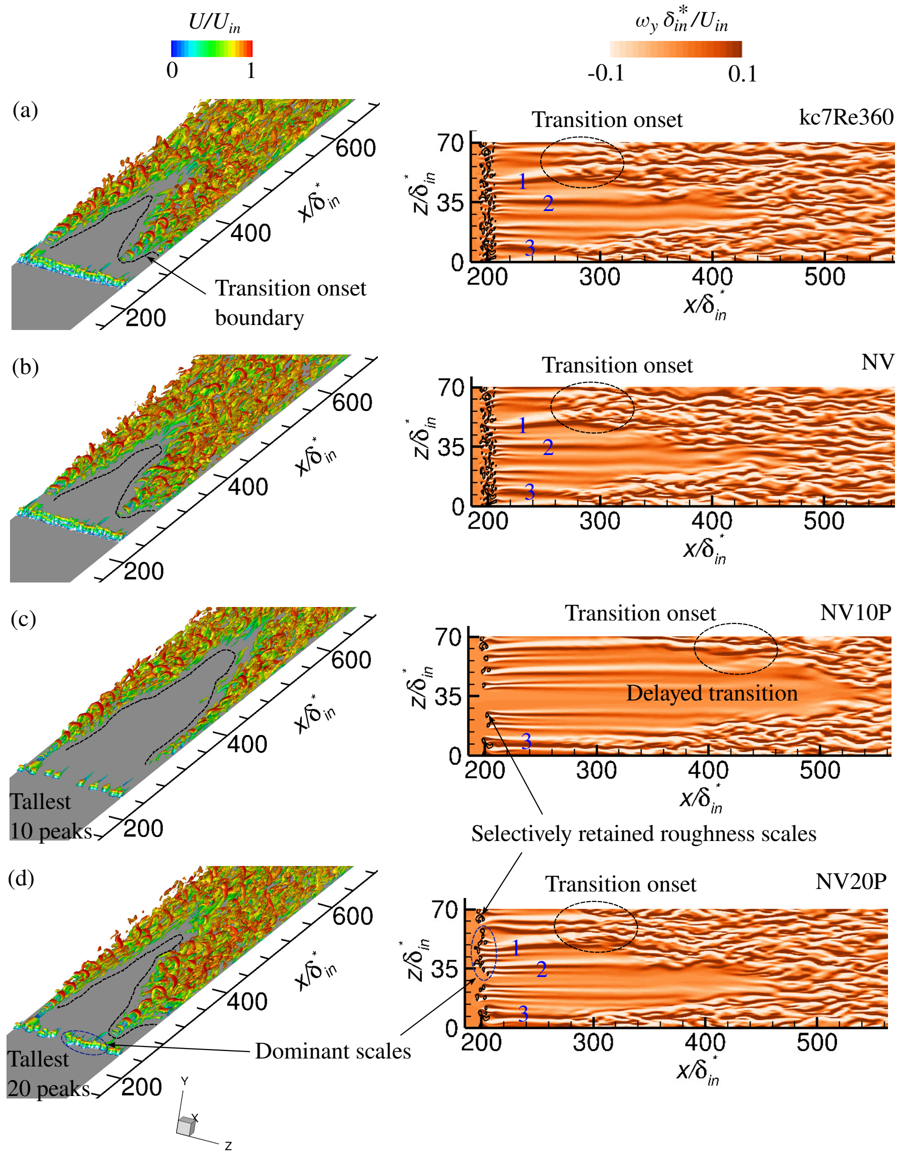

Fig. 14 Effect of selective retention of scales for $k_c = 7$ and $Re_{\delta^*_{in}} = 360$: (a) kc7Re360 (baseline), (b) NV, (c) NV10P and (d) NV20P. For each case, coherent structures visualized using Q iso-surfaces (Q=0.001) are shown on the left and instantaneous contours of wall-normal vorticity extracted at $\frac{y}{\delta} \approx 8\%$ (where δ is measured at $x/\delta^*_{in} = 200$) are shown on the right.

are 10 and 20 for the NV10P and NV20P surfaces, respectively. The higher the cut-off height, the more the tip features of roughness are retained. A smaller cut-off value tends to incorporate features close to the roughness foothills. (2) the selected peaks shown in Figure 13(a) are then smoothed into the flat surface using a MATLAB filleting routine that smooths the surrounding region. For the NV surface, it is worth noting that since no peak features are cut off, no smoothing operation is required on the roughness features. Figure 13(b) shows the top view of the original $k_c = 7$ rough surface. Figures 13(c-e) compare the roughness patterns employed for the simulations in Table 3. It is evident from Figures 13(c-e) that the numerical treatment accurately preserves the intended roughness features selected from the original $k_c = 7$ surface.

Simulations reported in this section are carried out at a Reynolds number of $Re_{\delta^*_{in}} = 360$. For the $NV20P$ case, the height of the peaks ranges between $k/\delta^*_{in} = 1.18-3$. Hence, the Reynolds number based on the roughness peaks varies between $Re_k = 425$ to 1080. Figures 14(a-d) compare the transitional flow structures of the original kc7 roughness with the other derived rough surfaces with the aid of Q iso-surfaces and wall-normal vorticity contours. Figure 14(a) representing the kc7Re360 case is shown again for the ease of comparison. The approximate transition onset boundaries are drawn for each test case in Q iso-surfaces. It is evident that there is only a negligible variation in the transition onset boundary for the NV case with respect to that for the kc7Re360 case. The corresponding wall-normal vorticity contours also exhibit a similar variation. In the unsteady vorticity contours, the evidently stronger steady streaks (marked as 1, 2 and 3 in Figures 14(a, b)) retain their identity even in the absence of roughness valleys. This indicates that valleys play a negligible role in varying the vorticity evolution that affects the transition process. This behavior concurs with the finding of Jelly and Busse [16] that the role of valleys on roughness effects is much weaker. However, for the NV10P case, there is a significant variation in the transition onset compared to the baseline kc7Re360 and NV cases, particularly close to the centreline where only a few peaks have been retained. There is a noticeable delay in the transition implying that the features responsible for the transition behavior in the kc7 rough surface are not fully retained. The delayed transition is marked in the wall-normal vorticity contours of the NV10P case. On the other hand, when the tallest 20 peaks from the kc7 roughness are retained, there is a good agreement in the transition onset boundary for the NV20P case compared to the baseline kc7Re360 case. This is attributed to the fact that the dominant scales (marked in Figure 14(d)) responsible for the generation of steady streaks 1 and 2 are retained in the NV20P case but are absent in the NV10P case. These scales are responsible for the transition onset occurring at $x/\delta^*_{in} \approx 300$ for the kc7Re360, NV, and NV20P cases. It indicates that the key parameter governing transition is the local value of roughness height-based Reynolds number which varied between 425 to 1080 across the top 20 peaks. Nevertheless, it is also worth noting that the lack of roughness features between $25 \leq z/\delta^*_{in} \leq 40$ for the NV10P case (see Figures 13(d) and 14(c)) delay the transition onset. It implies that apart from the roughness Reynolds number, the solidity or the number density of roughness features also plays a vital role in dictating the transition process. Hence, a transition pattern similar to NV and NV20P cases could be reproduced if the roughness elements were chosen based on both height and solidity. Further investigation on the effects of solidity is in progress which will be reported elsewhere.

The impact of selective retention of roughness features is now examined by considering the time-averaged flow statistics. Figures 15(a-d) present the contours of the maximum turbulent kinetic energy (TKE_{max}) for the kc7Re360, NV, NV10P and NV20P cases, obtained by projecting the TKE_{max} values onto a wall-normal plane.

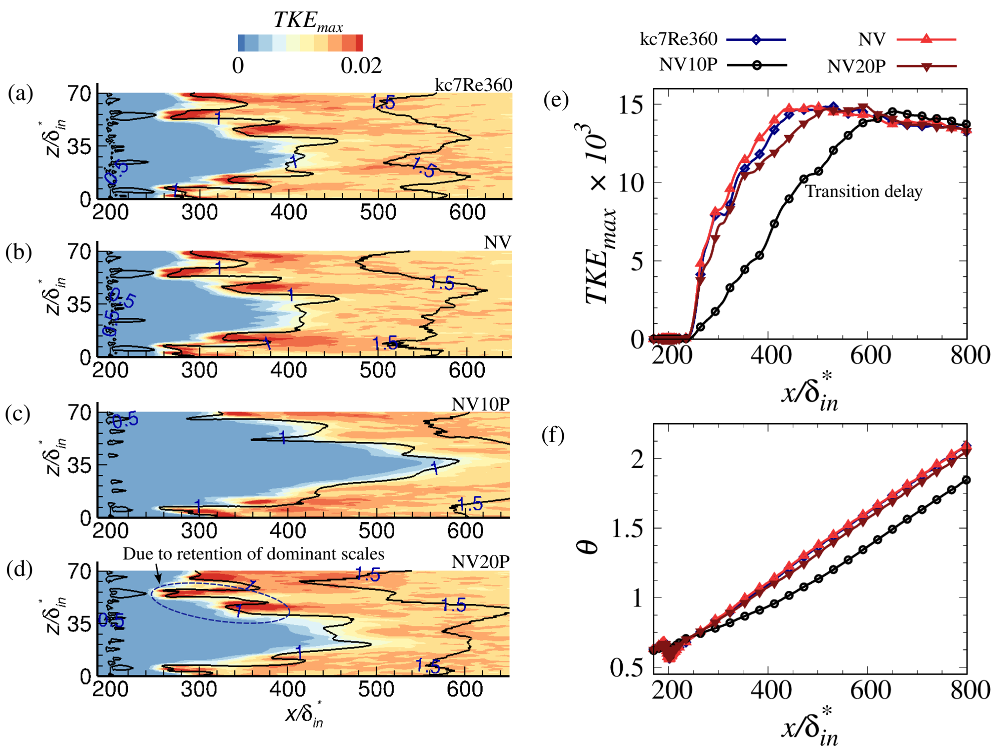

Fig. 15 Contours showing the distribution of maximum turbulent kinetic energy for (a) kc7Re360, (b) NV, (c) NV10P and (d) NV20P cases. Momentum thickness lines are overlaid for each case. Streamwise variation of span-averaged (e) maximum turbulent kinetic energy and (f) momentum thickness.

Overlaid on these contours are lines of constant momentum thickness, θ (the constant θ values are marked in the contours). The $\theta = 1$ line accurately captures the time-averaged transition onset boundary for all the cases. The location of the transition onset close to the periodic boundaries (depicted by regions of high TKE_{max} values) concurs well with the birth of hairpin structures and instantaneous vorticity in Figures 14(a-d). It is clear that the $\theta = 1$ line closely captures regions of high TKE_{max} and thus matches the approximate transition onset along span for all the cases. As noted in Figure 14(d) the case with 20 peaks (Figure 15(d)) accurately captures the transition onset boundary. Furthermore, the delayed transition in the NV10P case due to the absence of dominant peaks is also accurately depicted by the TKE_{max} contours and the $\theta = 1$ line in Figure 15(c). Figure 15(e) compares the streamwise variation of the span-averaged maximum turbulent kinetic energy for all the test cases. In the kc7Re360 and NV cases, the onset of turbulence occurs at $x/\delta^*_{in} \approx 450$. For the NV10P case, the delayed transition causes the turbulence onset to occur further downstream at $x/\delta^*_{in} \approx 650$. But when the dominant scales are retained for the NV20P case, the onset location shifts upstream to $x/\delta^*_{in} \approx 450$ thereby agreeing favourably with the kc7Re360 and NV cases. Figure 15(f) presents the streamwise variation of the span-averaged momentum thickness for the different cases. It is evident that except the NV10P case, all the cases show a quantitatively similar θ variation with only a marginal difference for the NV20P case from the baseline kc7Re360 case.

3.4 Impact of peaks from different rough surfaces

In this section, the effects of roughness scales with differing mean-square height (k_{rms}) and roughness frequencies (see Table 1) on transition are investigated based on the kc3Re360 and kc7Re360 cases. Note that the roughness valleys are ignored based on our earlier discussion in section 3.3.

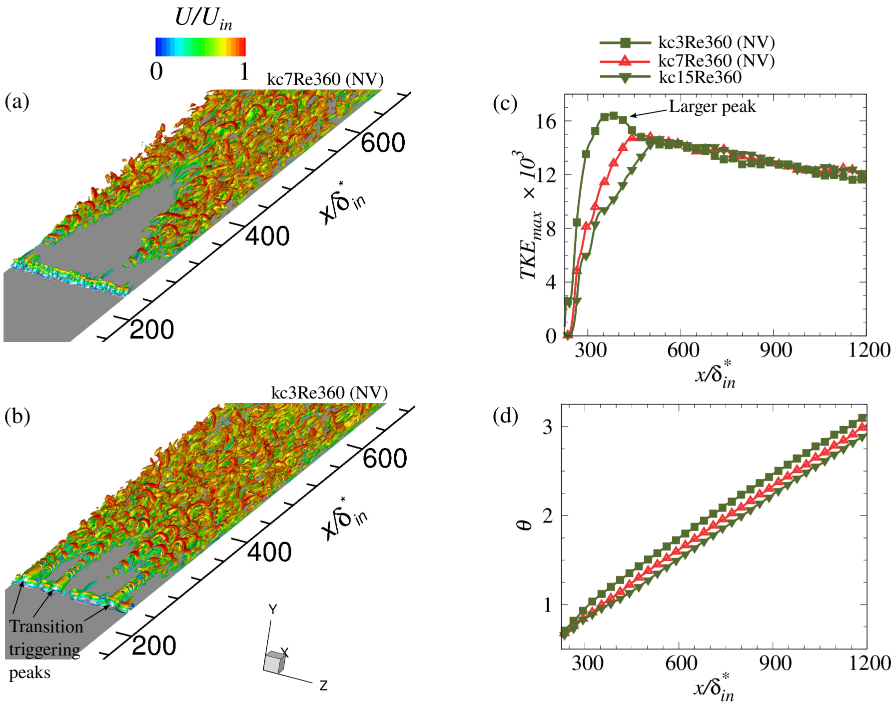

Fig. 16 Effect of roughness peaks on the transition onset for $k_c = 7$ and 3 surfaces at $Re_{\delta^*_{in}} = 360$: Transitional flow structures visualized using Q iso-surfaces (Q=0.001) over the (a) $k_c = 7$ roughness and (b) $k_c = 3$ roughness. Streamwise evolution of (c) maximum turbulent kinetic energy and (d) momentum thickness.

Figures 16(a) and (b) compare the coherent structures developing over the $k_c = 7$ and $k_c = 3$ roughnesses with the aid of Q iso-surfaces. The NV case from Figure 14(b) is repeated here for comparison. It is clear that when the roughness frequency is reduced from 7 to 3, an early transition is triggered as evident from the upstream shift in the transition onset boundary in Figure 16(b). The developing vortical structures over the dominant roughness peaks promoting transition (marked in the figure) are clearly visible. In line with our earlier observation in section 3.1, as the roughness frequency reduces the combined effect of stronger vortices developing around the sparsely packed features and reduced sheltering promotes an early transition. Figure 16(c) further elucidates this effect by comparing the streamwise variation of the maximum turbulent kinetic energy for the two test cases. Not only is the transition onset shifted upstream but also a larger TKE_{max} peak is observable for the $k_c = 3$ rough surface. However, beyond $x/\delta^*_{in} \approx 450$, the TKE_{max} variation almost collapses for both the surfaces. Due to an early transition onset a consistently thicker boundary layer growth over the entire streamwise extent occurs over the $k_c = 3$ surface compared to the $k_c = 7$ roughness as observable from the streamwise variation of momentum thickness in Figure 16(d).

4 Conclusions

High-fidelity scale-resolving simulations are performed on a zero-pressure gradient laminar boundary layer to investigate the effects of real roughness scales on transition behavior. Two different roughness patches with differing frequency content are employed to investigate the effects of high roughness wavenumbers on transition behavior under varying Reynolds numbers. The flat plate and the roughness patches are represented using the BDIM.

The results show that the transition is predominantly affected by the Reynolds number, with a higher $Re_{\delta^*_{in}}$ promoting earlier transition. The transition onset boundary is sensitive to the frequency content of the roughness and the boundaries become much more distinct at low Reynolds numbers. In particular, an increase in the frequency content of roughness is shown to marginally delay the transition onset. The inclusion of finer roughness scales reduces the spacing between roughness features thereby constraining the development of horseshoe vortices. The streaks are therefore weaker due to the mutual sheltering effect and the finer scales are shown to promote spanwise inhomogeneity of flow in the transition region. This effect is found to be much more prominent at low Reynolds numbers. In contrast, filtering out the finer roughness scales results in an earlier transition onset due to the strong streaks developing from the horseshoe vortices wrapping around the lateral walls of the sparsely packed roughness features. It is observed that in the transition region, localised spots of enhanced TKE behind the roughness scales are associated with high wall-normal vorticity.

The skin-friction distribution over the roughness patches shows that smaller roughness peaks situated on the leeward side of taller peaks experience reduced shear thereby confirming the existence of the sheltering effect among the roughness features. To investigate the impact of roughness sheltering, the kc7Re360 case is chosen as the baseline configuration, and further simulations are performed based on the rough surfaces derived from the kc7 roughness at $Re_{\delta^*_{in}} = 360$. It turns out that the roughness valleys play a negligible role in promoting transition. Furthermore, due to the sheltering effect, the influence of smaller peaks is limited and it is the tallest roughness peaks that dictate the transition process. The importance of the dominant peaks in accurately capturing the transition process becomes evident in both the instantaneous flow features and turbulent kinetic energy. This is demonstrated by comparing the NV20P case with the baseline kc7Re360 case. The minimal role played by the roughness valleys and smaller peaks shows that not all the roughness features need to be accurately resolved to predict the transition. In addition, for all the test cases examined, the new transition onset location (due to a change in roughness patch/Reynolds number) established quickly within $\approx 1725k_{rms}/U_{in}$ when the simulations are initialized with the flow field of kc15Re540. This is in contrast to the transition due to free-stream turbulence (FST). The intermittent nature of FST demands a longer time to flush out transients and longer statistical averaging to capture the transition onset. These critical observations (capturing the transition onset quickly with selective roughness scales) can be exploited to reduce the cost of the high-fidelity simulations leading to a significant computational benefit. It should also aid in developing better correlations for roughness-induced transition.

The present research has demonstrated the impact of real roughness scales on boundary layer transition with the aid of high-fidelity simulations. It became evident that the dominant roughness features that affect the transition process are the few tallest roughness peaks. Currently, efforts are underway by the authors to characterize these dominant scales which will aid in a systematic identification of the relevant scales for any given real roughness.

Appendix A Sensitivity of transition onset to roughness features

To ascertain the sensitivity of transition onset to roughness features, the kc15Re360 case is simulated by shifting the roughness patch along the span. The patch is shifted such that the scales closer to the periodic boundaries are re-positioned towards the center of the domain. Figure A1(a) depicts this shifting operation. Figure A1(b) compares the streamwise evolution of the time and span-averaged TKE_{max} before and after shifting. As expected the results are in close agreement with each other. Figures A1(c) and (d) compare the Q iso-surfaces for these test cases. For the kc15Re360 case, the transition gets triggered close to the periodic boundaries before shifting the roughness patch while the transition onset occurs close to the center of the domain for the shifted roughness patch. This further demonstrates that the sensitivity of transition onset to the roughness features is accurately captured.

Acknowledgements. The authors wish to acknowledge NVIDIA for generously donating an A100 GPU card. We thank P.G. Senapathy Centre, IIT Madras, and the National PARAM Supercomputing Facility (NPSF) for providing the computing resources on the PARAM Siddhi cluster under the National Supercomputing Mission. Dr. Nagabhushana Rao Vadlamani also acknowledges the Department of Science and Technology - Science and Engineering Research Board (DST-SERB) for funding the project [MTR/2022/000807].

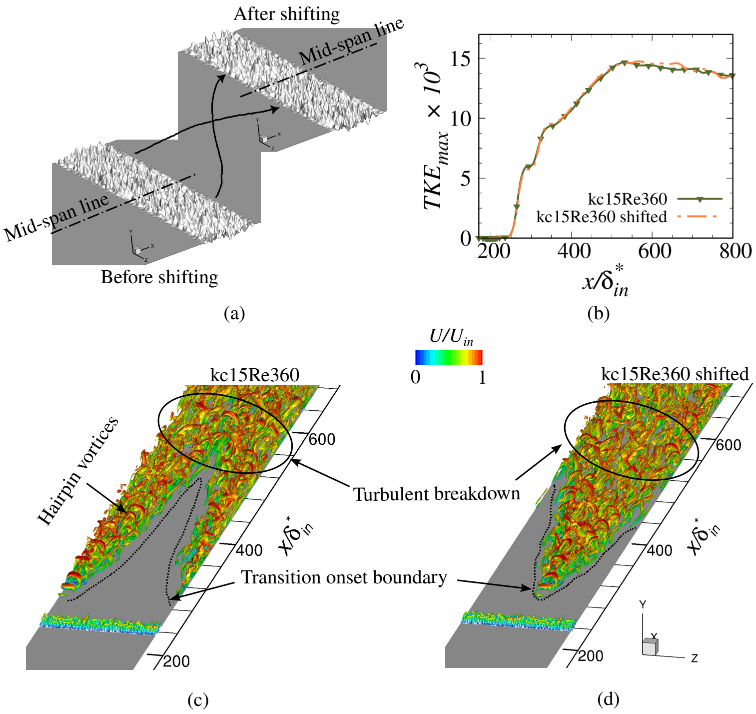

Fig. A1 Simulation of kc15Re360 case with and without spanwise shifting of roughness. (a) Layout of the roughness before and after shifting about the mid-span line, (b) time and span averaged maximum turbulent kinetic energy. Visualization of flow structures using Q iso-surfaces (Q=0.001) (c) kc15Re360, and (d) kc15Re360 shifted

Ethics Declarations

Funding:

Dr. Nagabhushana Rao Vadlamani also acknowledges the Department of Science and Technology - Science and Engineering Research Board (DST-SERB) for partly funding the project [MTR/2022/000807].

Conflict of interest:

The authors do not have any competing interests to declare that are relevant to the content of this article.

Ethical approval:

N/A

Informed consent:

N/A

Author contribution:

S.A: Conceptualization, Methodology, Investigation, Formal analysis, Data curation, Writing—review and editing, Visualization.
S.S.: Data curation, Formal analysis, Resources, Visualization
N.V: Conceptualization, Methodology, Supervision, Project administration, Funding acquisition, Writing—review and editing
J.C: Conceptualization, Methodology, Supervision, Project administration, Writing—review and editing

Data Availability Statement:

Data sets generated during the current study are available from the corresponding author on reasonable request.

References

[1] Bons, J.P.: A review of surface roughness effects in gas turbines. J. Turbomach. Trans. ASME **132**, 021004 (2010) https://doi.org/10.1115/1.3066315

[2] Ananth, S.M., Nardini, M., Vaid, A., Kozul, M., Vadlamani, N.R., Sandberg, R.D.: Profile loss reduction of high-lift turbine blades with rough and ribbed surfaces. J. Turbomach. Trans. ASME **145**(2), 021001 (2023) https://doi.org/10.1115/1.4055501

[3] Vadlamani, N.R., Jefferson-Loveday, R., Tucker, P.G., Lardeau, S.: Large eddy simulations in turbines: influence of roughness and free-stream turbulence. Flow. Turbul. Combust. **92**, 543–561 (2014) https://doi.org/10.1007/s10494-013-9465-9

[4] Schlichting, H., Gersten, K.: Boundary-Layer Theory. Springer, Heidelberg (2016)

[5] Stripf, M., Schulz, A., Bauer, H.-J., Wittig, S.: Extended models for transitional rough wall boundary layers with heat transfer—part i: Model formulations. J. Turbomach. Trans. ASME **131**, 031016 (2009) https://doi.org/10.1115/1.2992511

[6] Vadlamani, N.R., Tucker, P.G., Durbin, P.: Distributed roughness effects on transitional and turbulent boundary layers. Flow. Turbul. Combust. **100**, 627–649 (2018) https://doi.org/10.1007/s10494-017-9864-4

[7] Yuan, J., Piomelli, U.: Estimation and prediction of the roughness function on realistic surfaces. J. Turbul. **15**, 350–365 (2014) https://doi.org/10.1080/14685248.2014.907904

[8] Anand, A., Diwan, S.S.: Time-frequency analysis for two cases of boundary-layer transition induced by random distributed roughness. Exp. Fluids **61**, 1–14 (2020)

https://doi.org/10.1007/s00348-020-2895-y

[9] Jeong, H., Lee, S.W., Song, S.J.: Measurement of transitional surface roughness effects on flat-plate boundary layer transition. J. Fluids Eng. **141**(7), 074501 (2019) https://doi.org/10.1115/1.4042258

[10] Lu, Y., Liu, H., Liu, Z., Yan, C.: Investigation and parameterization of transition shielding in roughness-disturbed boundary layer with direct numerical simulations. Phys. Fluids **32**(7) (2020) https://doi.org/10.1063/5.0012464

[11] Deyn, L.H., Forooghi, P., Frohnapfel, B., Schlatter, P., Hanifi, A., Henningson, D.S.: Direct numerical simulations of bypass transition over distributed roughness. AIAA J. **58**(2), 702–711 (2020) https://doi.org/10.2514/1.J057765

[12] Muppidi, S., Mahesh, K.: Direct numerical simulations of roughness-induced transition in supersonic boundary layers. J. Fluid Mech. **693**, 28–56 (2012) https://doi.org/10.1017/jfm.2011.417

[13] De Marchis, M., Saccone, D., Milici, B., Napoli, E.: Large eddy simulations of rough turbulent channel flows bounded by irregular roughness: advances toward a universal roughness correlation. Flow. Turbul. Combust. **105**, 627–648 (2020) https://doi.org/10.1007/s10494-020-00167-5

[14] Yang, J., Stroh, A., Chung, D., Forooghi, P.: Direct numerical simulation-based characterization of pseudo-random roughness in minimal channels. J. Fluid. Mech. **941**, 47 (2022) https://doi.org/10.1017/jfm.2022.331

[15] Busse, A., Thakkar, M., Sandham, N.D.: Reynolds-number dependence of the near-wall flow over irregular rough surfaces. J. Fluid. Mech. **810**, 196–224 (2017) https://doi.org/10.1017/jfm.2016.680

[16] Jelly, T.O., Busse, A.: Reynolds and dispersive shear stress contributions above highly skewed roughness. J. Fluid. Mech. **852**, 710–724 (2018) https://doi.org/10.1017/jfm.2018.541

[17] Downs III, R.S., White, E.B., Denissen, N.A.: Transient growth and transition induced by random distributed roughness. AIAA J. **46**, 451–462 (2008) https://doi.org/10.2514/1.31696

[18] Sharma, A., Drews, S.D., Kuester, M., Goldstein, D.B., White, E.B.: Evolution of disturbances due to discrete and distributed surface roughness in initially laminar boundary layers. Paper presented at the AIAA SciTech Forum, 52nd Aerospace Sciences Meeting, 13–17 Jan (2014). https://doi.org/10.2514/6.2014-0235

[19] Kadivar, M., Tormey, D., McGranaghan, G.: A review on turbulent flow over rough surfaces: Fundamentals and theories. Int. J. Thermofluids. **10**, 100077 (2021) https://doi.org/10.1016/j.ijft.2021.100077

[20] Pinto, B., Lodato, G.: Synthetic freestream disturbance for the numerical reproduction of experimental zero-pressure-gradient bypass transition test cases. Flow. Turbul. Combust. **103**, 25–54 (2019) https://doi.org/10.1007/s10494-018-0004-6

[21] Rizzetta, D.P., Visbal, M.R.: Direct numerical simulation of transition control via local dynamic surface modification. AIAA J. **57**, 3309–3321 (2019) https://doi.org/10.2514/1.J057664

[22] Schlanderer, S.C., Weymouth, G.D., Sandberg, R.D.: The boundary data immersion method for compressible flows with application to aeroacoustics. J. Comput. Phys. **333**, 440–461 (2017) https://doi.org/10.1016/j.jcp.2016.12.050

[23] Ananth, S.M., Nardini, M., Vaid, A., Kozul, M., Vadlamani, N.R., Sandberg, R.D.: Riblet performance beneath transitional and turbulent boundary layers at low reynolds numbers. AIAA J. **61**, 1986–2001 (2023) https://doi.org/10.2514/1.J062418

[24] Sandberg, R.D., Sandham, N.D.: Nonreflecting zonal characteristic boundary condition for direct numerical simulation of aerodynamic sound. AIAA J. **44**, 402–405 (2006) https://doi.org/10.2514/1.19169

[25] Jelly, T.O., Busse, A.: Multi-scale Anisotropic Rough Surface Algorithm: Technical Documentation And User Guide. University of Glasgow, Glasgow (2019)

[26] Visbal, M.R., Gaitonde, D.V.: High-order-accurate methods for complex unsteady subsonic flows. AIAA J. **37**(10), 1231–1239 (1999) https://doi.org/10.2514/2.591

[27] Schlatter, P., Qiang, L., Brethouwer, G., Johansson, A.V., Henningson, D.S.: Simulations of spatially evolving turbulent boundary layers up to reθ= 4300. Int. J. Heat Fluid Fl. **31**, 251–261 (2010) https://doi.org/10.1016/j.ijheatfluidflow.2009.12.011

[28] Gaitonde, D.V., Visbal, M.R.: Padé-type higher-order boundary filters for the navier-stokes equations. AIAA J. **38**(11), 2103–2112 (2000) https://doi.org/10.2514/2.872

[29] Wenzel, C., Björn, S., Kloker, M., Ulrich, R.: Dns of compressible turbulent boundary layers and assessment of data/scaling-law quality. J. Fluid. Mech. **842**, 428–468 (2018) https://doi.org/10.1017/jfm.2018.179

[30] Schlatter, P.: Boundary Layer DNS/LES Data. https://www.mech.kth.se/~pschlatt/DATA/ (2012)

[31] Yang, X.I.A., Sadique, J., Mittal, R., Meneveau, C.: Exponential roughness layer and analytical model for turbulent boundary layer flow over rectangular-prism roughness elements. J. Fluid. Mech. **789**, 127–165 (2016) https://doi.org/10.1017/jfm.2015.687

[32] Hack, M.J.P., Zaki, T.A.: Streak instabilities in boundary layers beneath free-stream turbulence. J. Fluid. Mech. **741**, 280–315 (2014) https://doi.org/10.1017/jfm.2013.677

[33] Jacobs, R.G., Durbin, P.A.: Simulations of bypass transition. J. Fluid. Mech. **428**, 185–212 (2001) https://doi.org/10.1017/S0022112000002469

[34] Ergin, F.G., White, E.B.: Unsteady and transitional flows behind roughness elements. AIAA J. **44**, 2504–2514 (2006) https://doi.org/10.2514/1.17459

[35] Ganesh, N., Ananth, S.M., Vaid, A., Vadlamani, N.R., Rengarajan, S., Kontis, K.: Surface roughness effects on cavity flows. Flow. Turbul. Combust. **109**, 1215–1239 (2022) https://doi.org/10.1007/s10494-022-00345-7